nIFTy galaxy cluster simulations I: dark matter & non-radiative models

Federico Sembolini,[1,2,⋆] Gustavo Yepes,[1] Frazer R. Pearce,[3] Alexander Knebe,[1]
Scott T. Kay,[4] Chris Power,[5] Weiguang Cui,[5] Alexander M. Beck,[6,7,8] Stefano Borgani,[9,10,11]
Claudio Dalla Vecchia,[12,13] Romeel Davé,[14,15,16] Pascal Jahan Elahi,[17] Sean February,[18]
Shuiyao Huang[27] Alex Hobbs,[19] Neal Katz[19] Erwin Lau,[20,21] Ian G. McCarthy,[22]
Guiseppe Murante,[9] Daisuke Nagai,[20,21,23] Kaylea Nelson,[21,23] Richard D. A. Newton,[5,6]
Ewald Puchwein,[24] Justin I. Read,[25] Alexandro Saro,[14] Joop Schaye, [27] Robert J. Thacker[28]

[1] *Departamento de Física Teórica, Módulo 8, Facultad de Ciencias, Universidad Autónoma de Madrid, 28049 Madrid, Spain*
[2] *Dipartimento di Fisica, Sapienza Università di Roma, Piazzale Aldo Moro 5, I-00185 Roma, Italy*
[3] *School of Physics & Astronomy, University of Nottingham, Nottingham NG7 2RD, UK*
[4] *Jodrell Bank Centre for Astrophysics, School of Physics and Astronomy, The University of Manchester, Manchester M13 9PL, UK*
[5] *International Centre for Radio Astronomy Research, University of Western Australia, 35 Stirling Highway, Crawley, Western Australia 6009, Australia*
[6] *University Observatory Munich, Scheinerstr. 1, D-81679 Munich, Germany*
[7] *Max Planck Institute for Extraterrestrial Physics, Giessenbachstr. 1, D-85748 Garching, Germany*
[8] *Max Planck Institute for Astrophysics, Karl-Schwarzschild-Str. 1, D-85741 Garching, Germany*
[9] *Astronomy Unit, Department of Physics, University of Trieste, via G.B. Tiepolo 11, I-34143 Trieste, Italy*
[10] *INAF - Osservatorio Astronomico di Trieste, via G.B. Tiepolo 11, I-34143 Trieste, Italy*
[11] *INFN - Sezione di Trieste, via Valerio 2, I-34127 Trieste, Italy*
[12] *Instituto de Astrofísica de Canarias, C/ Vía Láctea s/n, 38205 La Laguna, Tenerife, Spain*
[13] *Departamento de Astrofsíca, Universidad de La Laguna, Av. del Astrofísico Franciso Sánchez s/n, 38206 La Laguna, Tenerife, Spain*
[14] *Physics Department, University of Western Cape, Bellville, Cape Town 7535, South Africa*
[15] *South African Astronomical Observatory, PO Box 9, Observatory, Cape Town 7935, South Africa*
[16] *African Institute of Mathematical Sciences, Muizenberg, Cape Town 7945, South Africa*
[17] *Sydney Institute for Astronomy, A28, School of Physics, The University of Sydney, NSW 2006, Australia*
[18] *Center for High Performance Computing, CSIR Campus, 15 Lower Hope Street, Rosebank, Cape Town 7701, South Africa*
[19] *Astronomy Department, University of Massachusetts, Amherst, MA 01003, USA*
[20] *Institute for Astronomy, Department of Physics, ETH Zurich, Wolfgang-Pauli-Strasse 16, CH-8093, Zurich, Switzerland*
[21] *Department of Physics, Yale University, New Haven, CT 06520, USA*
[22] *Yale Center for Astronomy and Astrophysics, Yale University, New Haven, CT 06520, USA*
[23] *Astrophysics Research Institute, Liverpool John Moores University, 146 Brownlow Hill, Liverpool L3 5RF, UK*
[24] *Department of Astronomy, Yale University, New Haven, CT 06511, USA*
[25] *Institute of Astronomy and Kavli Institute for Cosmology, University of Cambridge, Madingley Road, Cambridge CB3 0HA, UK*
[26] *Department of Physics, University of Surrey, Guildford, GU2 7XH, Surrey, United Kingdom*
[27] *Leiden Observatory, Leiden University, P.O. Box 9513, 2300 RA Leiden, the Netherlands*
[28] *Department of Astronomy and Physics, Saint Mary's University, 923 Robie Street, Halifax, Nova Scotia, B3H 3C3, Canada*

ABSTRACT

We have simulated the formation of a galaxy cluster in a ΛCDM universe using twelve different codes modeling only gravity and non-radiative hydrodynamics (ART, AREPO, HYDRA and 9 incarnations of GADGET). This range of codes includes particle based, moving and fixed mesh codes as well as both Eulerian and Lagrangian fluid schemes. The various GADGET implementations span traditional and advanced smoothed-particle hydrodynamics (SPH) schemes. The goal of this comparison is to assess the reliability of cosmological hydrodynamical simulations of clusters in the simplest astrophysically relevant case, that in which the gas is assumed to be non-radiative. We compare images of the cluster at $z = 0$, global properties such as mass, and radial profiles of various dynamical and thermodynamical quantities. The underlying gravitational framework can be aligned very accurately for all the codes allowing a detailed investigation of the differences that develop due to the various gas physics implementations employed. As expected, the mesh-based codes ART and AREPO form extended entropy cores in the gas with rising central gas temperatures. Those codes employing traditional SPH schemes show falling entropy profiles all the way into the very centre with correspondingly rising density profiles and central temperature inversions. We show that methods with

1   INTRODUCTION

Galaxy clusters are the largest virialized objects in the Universe and, as such, provide both an important testbed for our theories of cosmological structure formation and a challenging laboratory within which to study the fundamental physical processes that drive galaxy formation and evolution. The overdense regions that contain clusters in the present-day Universe were the first to collapse and virialize in the early Universe, and so our theories must predict their assembly history over a large fraction of the lifetime of the Universe (see Allen, Evrard & Mantz 2011 and Kravtsov & Borgani 2012 for a recent review). At the same time, galaxies in the cores of clusters have orbited within the often violently growing cluster potential over many dynamical times, while the broader cluster galaxy population is continually replenished by the infall of galaxies from the field.

Computer simulations are now well established as a powerful and indispensable tool in the interpretation of astronomical observations (see for instance Borgani & Kravtsov 2011). Early N-body simulations (White 1976; Fall 1978; Aarseth, Turner & Gott 1979), which included the gravitational effects of dark matter only, were vital in interpreting the results of galaxy redshift surveys and unveiling the large scale structure of the Universe, and subsequently in resolving structure in the non-linear regime of dark matter halo formation. The focus of modern simulations has now shifted to modeling galaxy formation in a cosmological context (see Borgani & Kravtsov 2011 for a recent review), incorporating the key physical processes that drive galaxy formation – such as the cooling of a collisional gaseous component (e.g. Pearce et al. 2000; Muanwong et al. 2001; Davé, Katz & Weinberg 2002; Kay et al. 2004; Nagai, Vikhlinin & Kravtsov 2007; Wiersma, Schaye & Smith 2009), the birth of stars from cool overdense gas (e.g. Springel & Hernquist 2003; Schaye & Dalla Vecchia 2008), the growth of black holes (Di Matteo, Springel & Hernquist, 2005), and the injection of energy into the inter-stellar medium by supernovae (e.g. Metzler & Evrard 1994; Borgani et al. 2004; Davé, Oppenheimer & Sivanandam 2008Dalla Vecchia & Schaye 2012) and powerful AGN outflows (e.g. Thacker, Scannapieco & Couchman 2006; Sijacki et al. 2007; Puchwein, Sijacki & Springel 2008; Sijacki et al. 2008; Booth & Schaye 2009). These processes span an enormous dynamic range, both spatial and temporal, from the sub-pc scales of black hole growth to the accretion of gas onto Mpc scales from the cosmic web. Galaxy clusters offer an ideal testbed for the study of these processes and their complex interplay, precisely because their enormous size encompasses the range of scales involved. For this reason, the study of galaxy formation and evolution in cluster environments occupies a fundamental position in observational and numerical astrophysics.

This raises the important question of how reliably cosmological galaxy formation simulations recover the properties of galaxy clusters. In the now classic Santa Barbara Cluster Comparison Project, Frenk et al. (1999) (SB99 from now on) compared the bulk dark matter and gas properties of a galaxy cluster formed in a non-radiative cosmological hydrodynamical simulation run using twelve (then state-of-the-art) mesh- and particle-based (hereafter smoothed particle hydrodynamics, SPH) codes. They displayed visual representations of the cluster at $z = 0$ and at $z = 0.5$ when

a major merger event was ongoing, and compared several observable quantities such as enclosed mass, gas temperature and X-ray emission. The large scatter in essentially all quantities between the twelve models is evident from the plots. The origin of these discrepancies was partly the poor timing agreement between the methods due to an ambiguity in the start redshift as well as large differences in the effective numerical resolution that arose because the simulation challenged the computing resources available at the time. The key discrepancy has, however, stood the test of times: the divergence between mesh-based and SPH codes in the radial entropy profile of the gas, defined in SB99 as

$$S(R) = \log \left[T_{\mathrm{gas}}(R)/\rho_{\mathrm{gas}}(R)^{2/3} \right] \tag{1}$$

where R is the spherical radius with respect to the cluster centre of mass; T_{gas} is the gas temperature; and ρ_{gas} is the gas density. Fig.18 of SB99 showed some tentative indication that the entropy profiles of the grid based codes (principally those of Bryan and Cen) displayed a constant entropy core whereas the entropy profiles of the sparticle based SPH codes continued to fall all the way into the centre.

These results have been confirmed subsequently by several studies (Voit, Kay & Bryan, 2005; O'Shea et al., 2005; Dolag et al., 2005; Wadsley, Veeravalli & Couchman, 2008; Mitchell et al., 2009). For example, Wadsley, Veeravalli & Couchman (2008) and Mitchell et al. (2009) suggested that the discrepancy owes also to the artificial surface tension and the associated lack of multiphase fluid mixing in classic SPH, while similar conclusions have been reached by Sijacki et al. (2012) when comparing the moving mesh code AREPO of Springel (2010) with classic SPH, using P-GADGET3 with the entropy conserving SPH version of Springel & Hernquist (2002). Interestingly, in their recent study, Power, Read & Hobbs (2014) have shown that SPHS (Read & Hayfield, 2012a), an extension of SPH that improves the treatment of mixing by means of entropy dissipation, produces constant entropy cores in non-radiative galaxy cluster simulations that are consistent with the results of the adaptive mesh refinement (AMR) code RAMSES (Teyssier, 2002). Both Wadsley, Veeravalli & Couchman (2008) and Maier et al. (2009) report entropy cores in runs that incorporate sub-grid models for turbulence. These results suggest that modern SPH codes can overcome the problems first reported in Frenk et al. (1999) and subsequently in Agertz et al. (2007). It is worth noting that it is not obvious that mesh-based codes necessarily recover the correct form for the entropy profile. For example, Springel (2010) reports significant variation in the entropy profile for the same AMR code (ENZO) that is particularly sensitive to choice of refinement criteria. More generally, differences are apparent when comparing AMR results to that of the moving mesh code AREPO Springel (2010) report an entropy core that is significantly lower than that found in AMR codes (e.g. compare Figure 45 of Springel 2010 with Figure 18 of Frenk et al. 1999 or Figure 5 of Voit, Kay & Bryan 2005).

In this work - emerging out of the 'nIFTy cosmology' workshop[1] - we revisit the idea of the Santa Barbara Cluster Comparison Project fifteen years later. We take four modern cosmological simulation codes (with one of them taken in nine different flavors, for a total of twelve different codes) and study the formation and evolution of a large galaxy cluster (with final mass $M_{200}^{\mathrm{crit}} \simeq 1.1 \times 10^{15} \mathrm{M}_\odot$). First we perform blind dark matter only

---

⋆ E-mail: federico.sembolini@uam.es

Table 1. List of all the simulation codes participating in the nIFTy cluster comparison project.

Code name	Reference
CART	Rudd, Zentner & Kravtsov (2008)
AREPO	Springel (2010)
HYDRA	Couchman, Thomas & Pearce (1995)
GADGET:	Springel (2005)
G2-Anarchy	Dalla Vecchia et al. in prep.
G3-X	Beck et al. (2015)
G3-SPHS	Read & Hayfield (2012a)
G3-Magneticum	Hirschmann et al. (2014)
G3-PESPH	Huang et al. in prep.
G3-MUSIC	Sembolini et al. (2013)
G3-OWLS	Schaye et al. (2010)
G2-X	Pike et al. (2014)

simulations with the favored parameter sets of each group. The results from these show the typical scatter that is expected for currently published works in this area. We then use a common parameter set to align our gravitational framework before continuing to study non-radiative gas simulations. This allows us to focus solely on the differences between the models that arise due to the different hydrodynamical implementations. This also permits us to cleanly study the formation (or not) of a gas entropy core.

The rest of this paper is organized as follows: in Section 2 we briefly describe the twelve methods used in this study and supply tables listing parameter choices. In Section 3 we describe how our initial conditions were generated and chosen. The main results are presented in Section 4, which discusses the dark matter only simulations, and in Section 5, which presents the results from the non-radiative simulations. We discuss convergence and scatter among the different codes in Section 6. We summarize out results in Section 7. We present additional supporting material the Appendix.

2 THE CODES

The numerical codes used for this project can be divided into two main groups: mesh-based and SPH codes. The mesh based codes used in this work are ART (Kravtsov, Klypin & Khokhlov, 1997) and AREPO (Springel, 2010): the first one uses Eulerian hydrodynamics as the second one uses a moving unstructured mesh and can be considered almost Lagrangian. SPH codes use Lagrangian hydrodynamics: we used HYDRA (Couchman, Thomas & Pearce, 1995) and nine different versions of GADGET (Springel, 2005). Among SPH codes we can distinguish classic and modern SPH, defining the latter as codes that adopted an improved treatment of discontinuities. The codes employ different techniques to solve the evolution equations for a two-component fluid of dark matter and non-radiative gas coupled by gravity. To calculate gravitational forces, ART uses Adaptive Mesh Refinement (AMR), AREPO and GADGET are based on TreePM (Tree+Particle-Mesh) methods and HYDRA uses AP^{3}M (Adaptive Particle-Particle, Particle-Mesh). Gas particles are treated in the following ways: by means of SPH in GADGET and HYDRA, using a Voronoi mesh in Arepo, and using Eulerian AMR in ART.

The following short summaries detail the specifics of each simulation code contributing to this comparison (the reference author for each code is the person who run the simulation). We focus on key differences and novel aspects. Generalized descriptions of the individual codes can be found in their respective methods papers. Table 1 provides the standard reference for each code; Table 2 summarizes the key numerical parameters used for each run. Sec. 2.3 describes the main improvements made by modern SPH codes.

2.1 Mesh-based codes

CART (Nagai, Nelson & Lau)

ART (Adaptive Refinement Tree, ART) is an N-body plus hydrodynamics code with adaptive mesh refinement. The code solves the inviscid fluid dynamical equations using a second order accurate Godunov method with piecewise-linear reconstructed boundary states and the exact Riemann solver of Colella & Glaz (1985). The current version of the code used for this work is CART (Chicago-ART), which it is parallelized for distributed machines using MPI and features a flexible time-stepping hierarchy.

AREPO (Puchwein)

Arepo uses a Godunov scheme on an unstructured moving Voronoi mesh. The mesh cells move (roughly) with the fluid. The main differences to Eulerian AMR codes consist in that AREPO is almost Lagrangian and it is Galilean invariant by construction; furthermore, AREPO has automatic refinement for hydrodynamics and gravity and uses a Tree-PM gravity solver. The main difference to SPH codes is that the hydrodynamic equations are solved with a finite-volume Godunov scheme. In this work, we always use the total energy as a conserved quantity in the Godunov scheme rather than the entropy-energy formalism described in Springel (2010).

2.2 SPH codes

GADGET2-ANARCHY (Dalla Vecchia)

Gadget-Anarchy (G2-Anarchy) is an implementation of GADGET2 employing the pressure-entropy SPH formulation derived by Hopkins (2013). The artificial viscosity switch has been been implemented following Cullen & Dehnen (2010), whose algorithm allows precise detection of shocks and avoid excessive viscosity in pure shear flows. G2-Anarchy uses a purely numerical switch for entropy diffusion similar to the one of Price (2008), but without requiring any diffusion limiter. The kernel adopted is the C^2 function of Wendland (1995) with 100 neighbors, with the purpose of avoiding particle pairing (as suggested by Dehnen & Aly 2012). The time stepping adopted is described in Durier & Dalla Vecchia (2012).

GADGET3-X (Murante)

This project employs two versions of GADGET3-X (G3-X). The default code, GADGET3-X-Std (G3X-Std) is a standard version of GADGET3 with the cubic spline kernel, 64 neighbours, low-order viscosity and a shear flow limiter (Balsara, 1995) and no conduction. The improved version GADGET3-X-ArtCond (G3X-Art; Beck et al. 2015) is an advanced version of GADGET3 with the Wendland kernel functions (Dehnen & Aly, 2012) with 200/295 neighbours, artificial conductivity to promote fluid mixing following Price (2008) and Tricco & Price (2013), but with an additional limiter for gravitationally induced pressure gradients, a time-step

limiting particle wake-up scheme Pakmor et al. (2012) and a high-order scheme for gradient computation (Price, 2012), shock detection and artificial viscosity similar to Cullen & Dehnen (2010) and Hu et al. (2014). A companion paper (Beck et al., 2015) presents an improved hydrodynamical scheme and its performance in a wide range of test problems.

GADGET3-SPHS (Power)

GADGET3-SPHS (G3-SPHS) was developed to overcome the inability of classic SPH to resolve instabilities. It has been implemented in the GADGET3 code. The key differences with respect to standard GADGET3 are in the choice of kernel and in dissipation. Rather than the cubic spline kernel, G3-SPHS uses as an alternative either the HOCT kernel with 442 neighbors or the Wendland C4 kernel with 200 neighbors. A higher order dissipation switch detects, in advance, when particles are going to converge. If this happens, conservative dissipation is switched on for all advected fluid quantities. The dissipation is switched off again once particles are no longer converging. This ensures that all fluid quantities are single-valued throughout the flow by construction.

GADGET3-MAGNETICUM (Saro)

Magneticum (G3-Magneticum) is based on the entropy-conserving formulation of SPH (Springel & Hernquist, 2002). Higher order kernel based on the bias-corrected, sixth-order Wendland kernel (Dehnen & Aly, 2012) with 295 neighbors. Also included is a low viscosity scheme to track turbulence (Dolag et al., 2005) and isotropic thermal conduction with $1/20^{th}$ Spitzer (Dolag et al., 2004).

GADGET3-PESPH (February)

GADGET3-PESPH (G3-PESPH) is an implementation of GADGET3 with pressure-entropy SPH (Hopkins, 2013) which features special galactic wind models. The SPH kernel is an HOCTS (n=5) B-spline with 128 neighbors. The time dependent artificial viscosity is that of Morris & Monaghan (1997).

GADGET3-MUSIC (Yepes)

The original MUSIC runs (G3-MUSIC) were done with the GADGET3 code, based on the entropy-conserving formulation of SPH (Springel & Hernquist, 2002). GADGET3 employs a spline kernel (Monaghan & Lattanzio, 1985) and parametrize artificial viscosity following the model described by Monaghan (1997).

GADGET3-OWLS (McCarthy)

The GADGET3-OWLS (G3-OWLS) simulations were run using a version of the Lagrangian TreePM-SPH code GADGET3, which was significantly modified to include new subgrid physics for radiative cooling, star formation, stellar feedback, black hole growth and AGN feedback, developed as part of the OWLS/cosmo-OWLS projects (Schaye et al., 2010). Standard entropy-conserving SPH (Le Brun et al., 2014) was used with 48 neighbors.

GADGET2-X (Kay)

GADGET2-X (G2-X) is a modified version of the GADGET2 code (SP05), using the TreePM gravity solver and standard entropy-conserving SPH. It includes a number of sub-grid modules to model metal-dependent radiative cooling, star formation and feedback from supernovae and AGN.

HYDRA (Thacker)

Table 2. Key numerical parameters used for each run. Columns 2 and 3 list values for the Plummer-equivalent softening lengths for the DM particles in physical units; columns 4 and 5 the same but for the gas particles (where present); and column 6 the number of FFT cells along each side of the box. We use the label 'Adp' when adaptive force resolution is used.

Code name	ϵ_{DM}	ϵ_{DM}^{max}	ϵ_{gas}	ϵ_{gas}^{max}	N_{FFT}
CART	Adp	Adp	Adp	Adp	256
AREPO	33.0	5.5	Adp	Adp	512
G2-Anarchy	20.0	5.0	20.0	5.0	512
G3-X	8.0	6.0	8.0	6.0	256
G3-SPHS	5.0	5.0	Adp	Adp	1024
G3-Magneticum	11.25	3.75	3.75	3.75	256
G3-PESPH	5.0	5.0	5.0	5.0	256
G3-MUSIC	8.0	6.0	8.0	6.0	512
G3-OWLS	9.77	5.0	9.77	5.0	1024
G2-X	24.0	6.0	24.0	6.0	256
HYDRA	Adp	5.0	Adp	5.0	512

HYDRA-OMP (Hydra) (Thacker & Couchman, 2006) is a parallel implementation of the earlier serial HYDRA code (Couchman, Thomas & Pearce, 1995). Aside from the parallel nature of the code, HYDRA-OMP differs from the serial implementation by using the standard pair-wise artificial viscosity along with the Balsara modification for rotating flows. Otherwise, the SPH implementation is "classic" in nature, using 52 neighbors, and does not include more recently preferred kernels, terms for conduction or explicit shock tracking to modify the dissipation. It also uses a conservative time-stepping scheme that keeps all particles on the same synchronization.

2.3 Progresses with modern SPH codes

Since the first development of SPH by Gingold & Monaghan (1977) and Lucy (1977) great advancements have been made to improve the accuracy and stability of SPH simulations. In particular, much attention has been given to the treatment of discontinuities. Artificial viscosity is necessary for a proper fluid sampling at shocks and to prevent particle interpenetration. The first spatially constant low-order formulations of artificial viscosity applied viscosity not only in shocks, but also in shearing flows and un-shocked regions leading to an over diffusion of kinetic energy. Modern formulations of artificial viscosity rely on proper shock detection methods and high-order gradient estimators to distinguish between shocked and un-shocked or shearing regions (Morris & Monaghan, 1997; Cullen & Dehnen, 2010; Price, 2012; Hu et al., 2014). Most importantly, they preserve kinetic energy to a much higher degree and promote simulations of turbulence or hydrodynamical instabilities. Furthermore, SPH intrinsically fails to treat different gas phases and their mixing correctly, caused by the lack of diffusion terms and an always present spurious surface tension, as shown for instance by Agertz et al. (2007).

Read, Hayfield & Agertz (2010) showed that the mixing problem in SPH owes to two problems: the force inaccuracy and the lack of entropy mixing. Artificial conduction (Price, 2008) or pressure-entropy (Ritchie & Thomas, 2001; Saitoh & Makino, 2013; Hopkins, 2013) formulations have been developed to overcome these issues. They provide for the transport of heat between particles or change the basic physical variables. However, in the presence of gravitationally induced pressure and temperature gradients, artifi-

Table 3. SPH schemata used for the comparison runs. We list the employed kernel functions and number of neighbours (N_{SPH}) as well as the minimum smoothing length ($h_{\min}$) in terms of the gravitational softening length. Furthermore, we provides information about the artificial viscosity and conductivity switches.

Code name	Hydrodyn. Kernel	N_{SPH}	$h_{\min}$	Art. Visc.	Shearflow	Mixing	Limiter
G2-Anarchy	Wendland C2	100 ± 3	0	Adaptive	LowOrder	Artificial	Yes
G3-XArt	Wendland C6	295 ± 10	0.1	Adaptive	HighOrder	Artificial	Yes
G3-SPHS	Wendland C4	200 ± 0.5	1.0	Adaptive	LowOrder	Artificial	Yes
G3-Magneticum	Wendland C6	295 ± 0.5	0.001	Adaptive	HighOrder	Physical	-
G3-PESPH	HOCTS B-spline	128 ± 2	0.1	Adaptive	LowOrder	-	-
G3-MUSIC	Cubic spline	40 ± 3	0.1	Constant	LowOrder	-	-
G3-XStd	Cubic spline	64 ± 1	0.1	Constant	LowOrder	-	-
G3-OWLS	Cubic spline	48 ± 1	0.01	Constant	LowOrder	-	-
G2-X	Cubic spline	50 ± 3	1	Constant	LowOrder	-	-
HYDRA	Cubic spline	$53 \pm 1\,5$	0.5	Constant	LowOrder	-	-

cial conduction schemes might lead to unwanted transport of heat, making the use of numerical limiters as well as correction terms are highly desirable. Read & Hayfield (2012b) showed that pressure-entropy SPH fails for strong shocks and/or if the density gradient is large. This was significantly improved by Hopkins (2013) who derived a conservative pressure-entropy SPH for the first time. However, the problem with large density gradients remained. Read & Hayfield (2012b) propose instead to use higher order switching, similarly to Cullen & Dehnen (2010), but applied to all advected fluid quantities. This solved the mixing problem in SPH also for high density contrast and opened the door to "multimass" SPH for the first time.

Lastly, the commonly employed cubic spline kernel function can easily become unstable, which leads to the pairing instability, incorrect gradient estimators and a poor fluid sampling. Therefore, a change of kernel function is highly recommended, and Wendland kernels (Dehnen & Aly, 2012) are now commonly used to retain fluid sampling. Table 3 provides an overview of the different SPH codes participating in our cluster comparison project and lists their numerical details.

3 THE SIMULATION

The cluster we have adopted for this project was drawn from the MUSIC-2 sample (Sembolini et al. 2013; Sembolini et al. 2014; Biffi et al. 2014) which consists of a mass limited sample [2] of re-simulated halos selected from the MultiDark cosmological simulation (Prada et al., 2012). This simulation is dark-matter only and contains 2048^3 (almost 9 billions) particles in a $(1h^{-1}\mathrm{Gpc})^3$ cube. It was performed in 2010 using ART (Kravtsov, Klypin & Khokhlov, 1997) at the NASA Ames Research centre. All the data from this simulation are accessible online through the *MultiDark Database*.[3] The run was done using the best-fitting cosmological parameters to WMPA7+BAO+SNI ($\Omega_{\mathrm{M}} = 0.27$, $\Omega_{\mathrm{b}} = 0.0469$, $\Omega_{\Lambda} = 0.73$, $\sigma_8 = 0.82$, $n = 0.95$, $h = 0.7$, Komatsu et al. 2011). This is the reference cosmological model used in the rest of the paper.

The MUSIC-2 cluster catalogue was originally constructed by selecting all the objects in the simulation box which are more massive than 10^{15} $h^{-1}\mathrm{M}_\odot$ at redshift $z = 0$. In total, 282 objects were found above this mass limit. A zooming technique described in Klypin et al. (2001) was used to produce the initial conditions for the re-simulations. All particles within a sphere with a radius of 6 $h^{-1}\mathrm{Mpc}$ around the centre of each selected object at $z = 0$ were found in a low-resolution version (256^3 particles) of the MultiDark volume. This set of particles was then mapped back to the initial conditions to identify the Lagrangian region corresponding to a 6 $h^{-1}\mathrm{Mpc}$ radius sphere centered on the cluster centre of mass at $z = 0$. The initial conditions of the original simulations were generated on a finer mesh of size 4096^3. By doing so, the mass resolution of the re-simulated objects was improved by a factor of 8 with respect to the original simulations. In the high resolution region the mass resolution for the dark matter only simulations corresponds to $m_{\mathrm{DM}}=1.09\times10^9$ $h^{-1}\mathrm{M}_\odot$. For the runs with gas physics, $m_{\mathrm{DM}}=9.01\times10^8$ $h^{-1}\mathrm{M}_\odot$ and to $m_{\mathrm{gas}}=1.9\times10^8$ $h^{-1}\mathrm{M}_\odot$.

4 DARK MATTER RUN COMPARISON

We first completed a dark matter only simulation, performed using the parameter values given in Table 2. These were chosen independently by each modeling group following their previous experience. A visual comparison of the density field centered on the cluster at $z = 0$ is given in Figure 1. While it is clear that all the methods have followed the formation of the same object (with a significant improvement with respect to Figure 1 of SB99) the precise location of the major subhalo is not accurately recovered. For several methods it has already crossed R_{200}^{crit} (the radius enclosing an overdensity of 200 relative to the critical density) while in others it is still falling in. The variance across this figure illustrates the typical range of outcomes from commonly used cosmological codes. The major cause of the discrepancy (for the GADGET based codes at least) is the size of the base level particle mesh. Those implementations which employed a base mesh of 256^3 did not sufficiently resolve the interface region between this low resolution mesh and the higher resolution region placed over the cluster. Improving the resolution of the base level mesh to 512^3 alleviates this problem and aligns the dark matter component well. We demonstrate this by showing the effect of changing the size of the particle mesh for the G3-MUSIC code in the appendix (Figure 13) together with a similar set of visual images taken from the following non-radiative simulation when the simulation parameters influencing the accuracy of

---

[2] specifically, it is cluster 19 of MUSIC-2 dataset; all the initial conditions of MUSIC clusters are available at `http://music.ft.uam.es`
[3] www.MultiDark.org

the dark matter are aligned across the code. This demonstrates that, given a common set of parameters, the dark matter framework underlying the simulation can be made to look very similar (this is not surprising at least for the GADGET based codes and AREPO as they all use the same gravity solver).

Figure 2 displays the radially averaged projected dark matter density profiles for the 12 different non-aligned DM-only runs, including also the residuals relative to the density profile of the reference G3-MUSIC simulation. The secondary peak marks the location of the major subhalo, at $R \sim 1h^{-1}$Mpc, significantly closer to the centre in some simulations due to the size of the top level particle mesh employed. All the simulations except CART lie well within 10 per cent of each other at all radii with the HYDRA simulation being indistinguishable from the GADGET runs. CART produces a cluster that is slightly more centrally concentrated than for the particle based approaches, especially within the inner $100h^{-1}$kpc.

The subhalo mass function at $z = 0$ (Figure 3) is recovered with a very close agreement (differences are always below 20 per cent at all masses) by all codes. Subhalos here have been identified using AHF (Gill, Knebe & Gibson 2004; Knollmann & Knebe 2009; freely available from http://popia.ft.uam.es/AHF). The number of subhalos is essentially identical except for tiny mass differences which are driven by the small divergences in radial location that were identified above. These code to code variations lead to differences in the mass associated with each subhalo as the threshold that defines where a subhalo is separated from the background halo varies. As expected, subhalos closer to the centre of the main halo than the equivalent subhalo in one of the other models have a lower recovered mass.

Comparison of the dark matter distribution and of its radial density profile at $z = 1$ give results similar to those described above. We conclude that the typical range of chosen parameters for cosmological simulation codes introduces a variation of around 10 per cent in the density profile of collapsed objects. This scatter can be reduced to less than 5 per cent by aligning the numerical accuracy of our calculations. Although this is not essential for many applications, we choose to do this in the remainder of this paper so that, as we show in the appendix, the underlying dark matter framework agrees closely, allowing us to focus on differences resulting from the various hydrodynamical schemes.

5   NON-RADIATIVE RUN COMPARISON

We now proceed to include a gas phase into our calculations. We repeat the simulation of the same cluster as used in Section 4 including gas which however we do not allow to radiate energy. Figure 4 shows some of the global properties of the selected cluster as calculated by the different codes used in this work: radius, mass, mass-weighted temperature, gas fraction, dark matter velocity dispersion and axial ratios. All these quantities have been calculated at an aperture radius corresponding to R_{200}^{crit}, the radius enclosing an overdensity of 200 relative to the critical density, defined as

$$\rho_c(z) = \frac{3H_0^2 E(z)^2}{8\pi G} \tag{2}$$

where H_0 is the present value of the Hubble constant, G is the universal gravitational constant – using the same definition we refer in the text to R_{2500}^{crit} and R_{500}^{crit} as the radii enclosing an overdensity of 2500 and 500 to $\rho_c(z)$. It is interesting to note that all the codes

were able to recover the same values for the different properties of the halo with a scatter smaller than 1 per cent for mass, radius, axial ratio and dark matter velocity dispersion and around 2 per cent for baryon fraction and gas temperature. The same properties were estimated with a scatter between 5 and 10 per cent in SB99, with differences of up to 30 per cent between the maximum and minimum values: in our comparison the same difference is always below 5 per cent (only for the gas fraction we register a disagreement of 8 per cent between the maximum and minimum values).

Thumbnail images of the gas density distribution for each of the methods at $z = 0$ are given in Figure 5. We see a dramatic variation in the central concentration of the gas, with some methods having significantly larger extended nuclear gas regions.

This trend is born out by the radial gas density profiles given in Figure 6. We see that the radial gas density is significantly more extended for CART and AREPO when compared to the traditional SPH schemes employed by some SPH codes such as HYDRA and G2-X. SPH codes that implement artificial diffusion are quite close to CART and AREPO. Lagrangian methods with entropy mixing (including AREPO which is Lagrangian in spirit) are always very close to each other, while CART produces a gas density profile that is shallower in the central regions and steeper at larger radii.

The difference in the radial gas density compared to the fiducial G3-MUSIC run are shown in the top panel of Figure 6. All the residuals are calculated to the density profile of the reference G3-MUSIC simulation (and we adopt this definition for all the radiative profiles shown from now on). At $z = 0$ the lowest central densities are an order of magnitude lower than in the G3-MUSIC simulation while the highest central densities are around 5 times larger. i.e. the variation in the central gas density across our runs is nearly two orders of magnitude. The scatter becomes more moderate when considering the outer region of the cluster, not exceeding 20 per cent at radii larger than R_{2500}^{crit}.

We next show the radial temperature profiles for all the simulations in Figure 7. We use the mass-weighted temperature, defined as:

$$T_{mw} = \frac{\sum_i T_i m_i}{\sum_i m_i} \tag{3}$$

where m_i and T_i are the mass and the electronic temperature of the gas particles . The central temperatures vary by more than a factor of 3, with a group of methods displaying a central temperature inversion with inner temperatures around half the peak value of 7-8 keV. In contrast, some codes display a monotonically rising temperature profile as the radius falls with a peak temperature up to 14 keV at the very centre. This group of codes consists of those with the most extended radial gas density profiles. Also in this case CART results are different from AREPO and SPH with thermal diffusion. It is interesting that the jump in temperature seen at ~ 1 h^{-1}Mpc for all Lagrangian methods is not seen by CART, probably because in this case the substructure that causes this bump is located in a slightly different halo position due to the differences in the merger phase. At radii larger than R_{2500}^{crit} the scatter is significantly more moderate, and the residuals appear to be a factor of 2 smaller than in Figure 17 of SB99 in the same cluster regions.

Finally we show the radial gas entropy profiles for all the codes in Figure 8. We adopt the definition of entropy commonly used in the literature by works on X-ray observations:

$$S(R) = \frac{T_{gas}(R)}{n_e^{2/3}(R)} \tag{4}$$

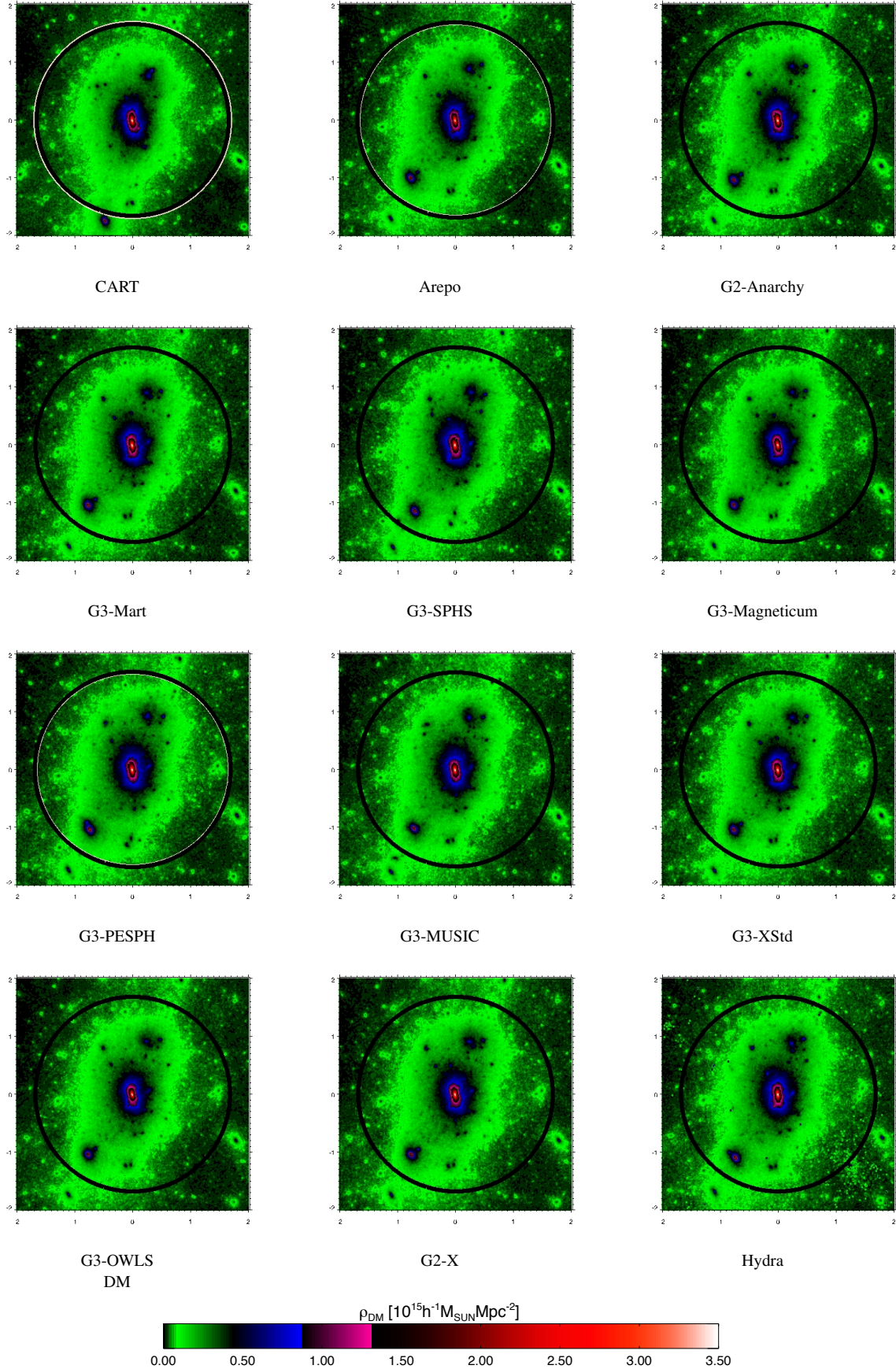where n_e is the number density of free electrons of the gas. This

Figure 1. Projected density of the dark matter halo at $z = 0$ for each simulation as indicated. The box is $2h^{-1}$Mpc on a side. The white circle indicates M_{200}^{crit}
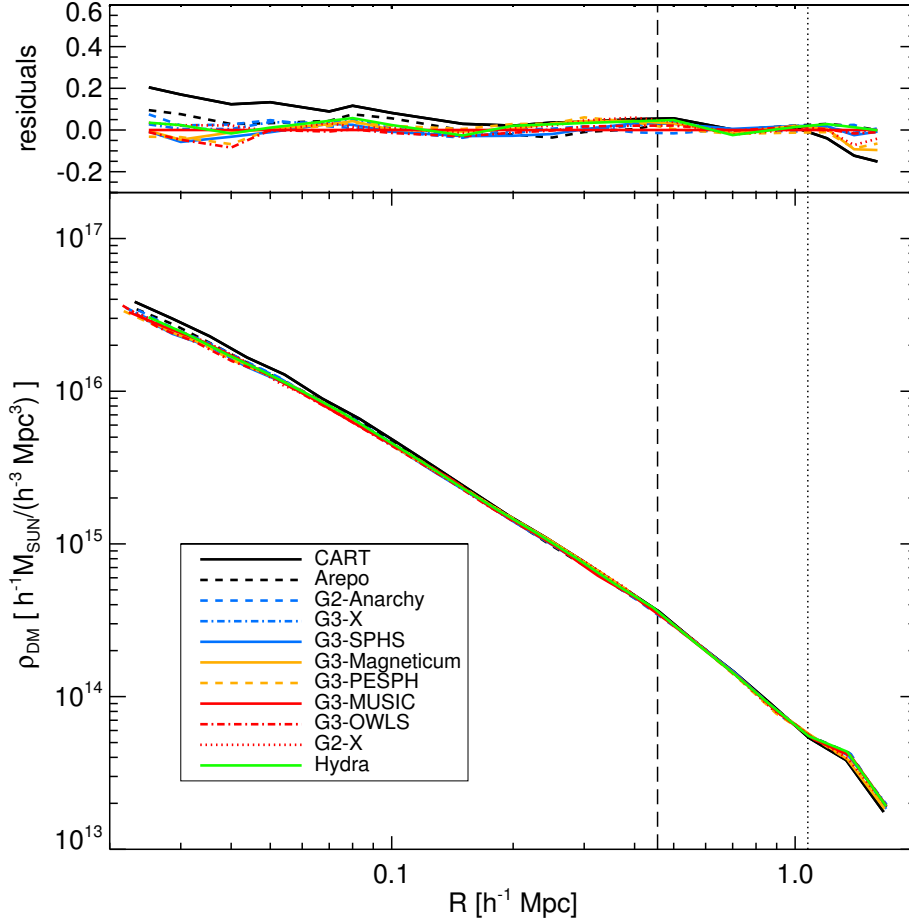
Figure 2. Radial density profiles for the dark matter only simulations at $z = 0$ (bottom panel) and difference between the radial density profiles of each dark matter only simulations at $z = 0$ and the reference G3-MUSIC density profile (top panel). The vertical dashed line corresponds to R_{2500} and vertical dotted line to R_{500} of the reference G3-MUSIC values.

displays the now classic split between grid-based codes and traditional SPH methods, such as HYDRA and G2-X, which show a falling inner entropy as the radius is decreased all the way into the very centre. This is completely consistent with the inner temperature inversion and high central density. Conversely, the grid-based codes such as CART and AREPO display the well known flat inner entropy cores that result from rising inner temperature profiles and extended gas densities. However, we see that in between these extremes we have a full range of entropy profiles that depend on the specific SPH implementation employed. Differently from what was shown in SB99 (see their Figure 18) modern, sophisticated SPH codes which employ mixing are now capable of recovering entropy profiles that lie anywhere between the core-less traditional SPH schemes and the cored profiles of the grid-based approaches depending upon the precise nature of the scheme and the amount of mixing employed. We highlight that modern SPH codes such as G3-SPHS, G2-Anarchy and G3-XArt are able to recover the same flat entropy core observed for CART and AREPO with a scatter smaller than 20 per cent, even in the inner cluster regions. G3-PESPH and G3-Magneticum, which have artificial viscosity switch but different artificial conductivity with respect to the other modern SPH codes, show and intermediate behavior between standard and modern SPH codes.

5.1 Other quantities in the non-radiative simulations

It is important to note that the differences in radial gas density, temperature and entropy evidenced above are not driven by code issues such as poor thermalization or large scale flows. In Figure 9 we show the ratio of gas thermal U to kinetic energy K at $z = 0$:

$$\eta = \frac{2K}{|U|} \qquad (5)$$

radial profile of all the simulations. All the methods agree closely on the value of η as a function of halo radius and none display any evidence of poor thermalization. Interestingly, we note that CART is the most efficient in converting kinetic energy into thermal energy (though also the different merger phase may contribute to this offset). Even considering the difference between CART and the other codes, the scatter is always below 20 per cent.

Given our radial dark matter density and gas density profiles we can also calculate the radial gas fraction for all the methods. In Figure 10 we show the radial profiles of the depletion factor Υ, defined as:

$$\Upsilon = \frac{M_{gas}(< R)}{M(< R)} \cdot \left(\frac{\Omega_b}{\Omega_m} \right)^{-1} \qquad (6)$$

The results reflects the existence of methods that produce very centrally concentrated gas and methods yielding an extended core with
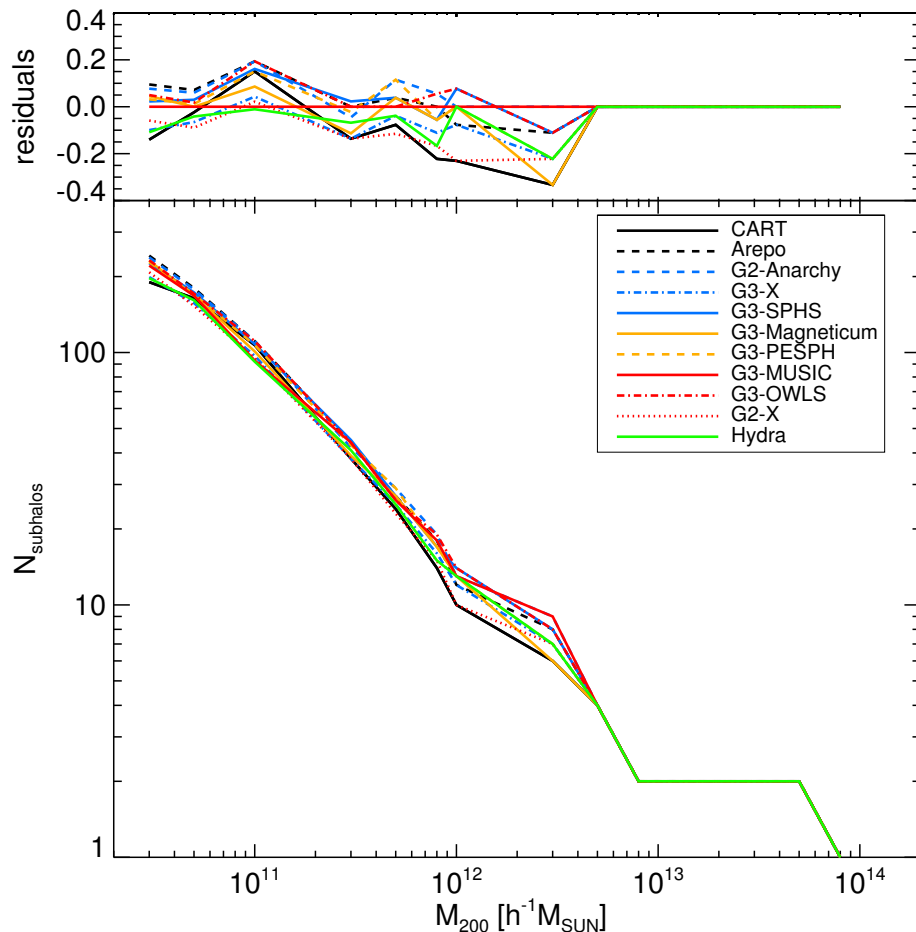
Figure 3. Subhalo mass function for the dark matter only simulations at $z = 0$ (bottom panel) and difference between the subhalo mass function of each dark matter only simulations at $z = 0$ and the reference G3-MUSIC subhalo count (top panel).

much higher average entropy. For those codes with an extended entropy core the gas fraction falls significantly with decreasing radius and can reach values as low as 5 per cent of the Universal baryon fraction for these non-radiative simulations. Within $100h^{-1}$kpc it can fall below 25 per cent of the cosmic gas fraction in both grid-based and modern SPH codes. The differences in the radial gas fraction reflect those detected in the gas density profiles and warn about using a universal calibration of the baryon depletion at R_{2500}^{crit} based on simulations in cosmological applications of the cluster baryon fraction, especially when using only non-radiative gas. We expect these results to be very different (and closer to observational results) when radiative physics is included. The scatter in the outer regions of the cluster appear by the way to be much more limited (less than 20 per cent) with respect to the results shown in Figure 13 of SB99, where differences of up to 50 per cent between the different codes where registered even close to the virial radius.

We can combine our measurements of the gas density and temperature to produce Figure 11, the gas pressure profiles and Figure 12, the X-ray emission profiles. We define the pressure as $P = \rho_{gas}T$ and we normalize the profiles to the value of P_{500} (the value of the pressure as calculated at R_{500}^{crit}) in order to be consistent with the definition of universal pressure profile introduced by Arnaud et al. (2010). The X-ray luminosity profile is defined as $4\pi R^3 L_X$ and we approximate the X-ray luminosity density as $L_X = \rho_{gas}^2 T^{1/2}$. The variation in the gas density and temperature

produce very different pressure and X-ray emission profiles. As expected, the pressure profiles continue to rise all the way into the centre for all codes (as the central gas is close to hydrostatic equilibrium in all cases). Due to the very high central density, the central X-ray emission for HYDRA is over two orders of magnitude higher than that found by the grid-based and some modern SPH methods which form extended cores. The differences observed in CART profiles, especially in Figure 11, can be attributed to the different merger phase.

6 CONVERGENCE AND SCATTER BETWEEN SIMULATIONS

6.1 Dark matter only runs

The major cause of the discrepancy (for the GADGET based codes at least) is the size of the base level particle mesh. A base mesh of 256^3 is not sufficient to resolve the interface region between the low resolution region (i.e. the base level) and the high resolution region (i.e. the refined level) placed over the cluster; we found that a base level of at least 512^3 is required to ensure that the dark matter component is well aligned across the different codes. For the N-body only simulations we find excellent agreement between the density profiles of the main halo and the statistics of their subhalos (Figures 2 and 3), once the input parameters of the various runs
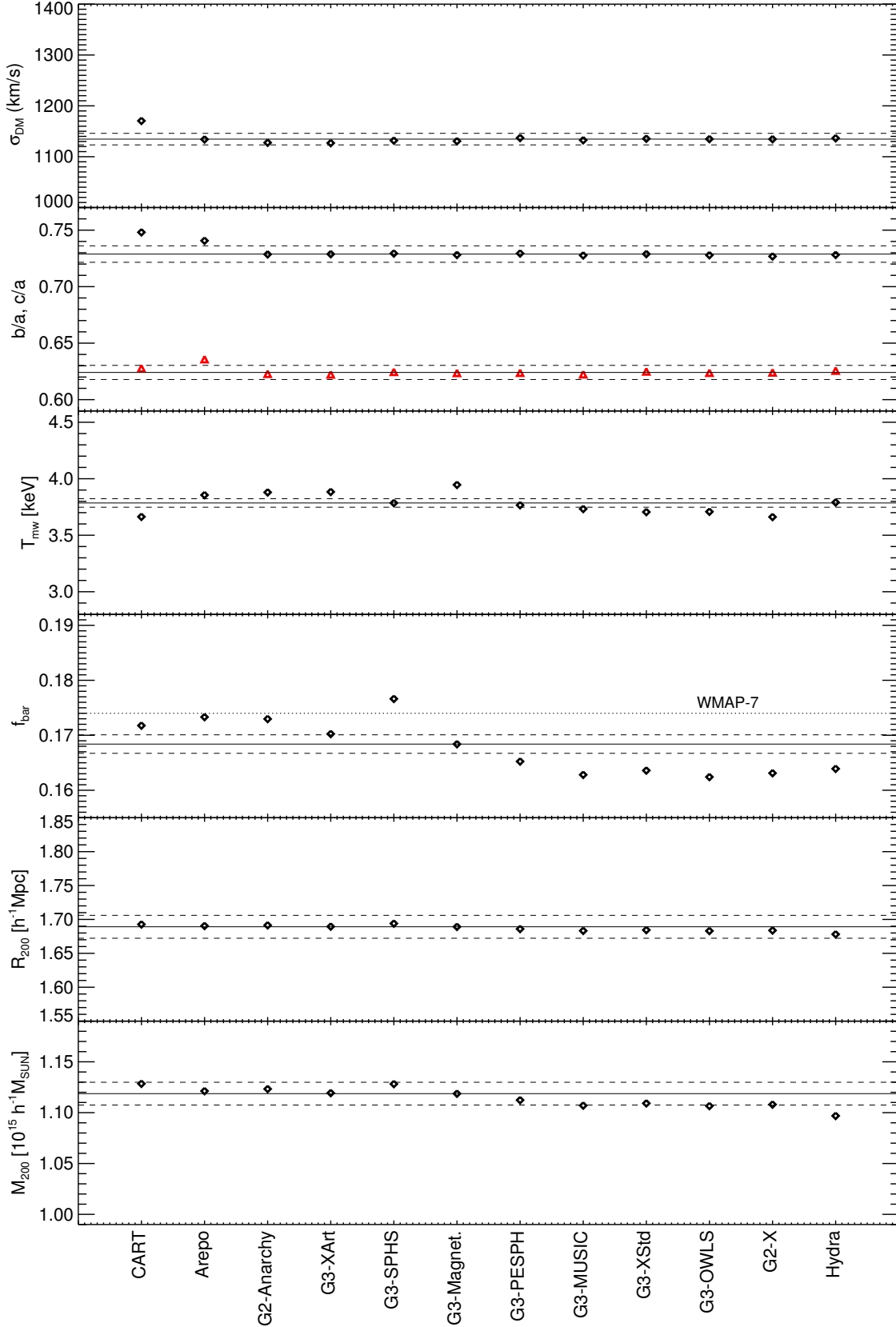
Figure 4. Global properties of the cluster calculated by the different codes. All quantities are computed within R_{200}^{crit}. From top panel to bottom panel: (1) the one-dimensional dispersion of the dark matter, (2) the axial ratio (b/a in black, c/a in red), (3) the mass-weighted temperature, (4) the gas fraction (dotted line represented the value of the cosmic ratio from WMAP7 (Komatsu et al., 2011), (5) the radius and (6) the total cluster mass. The solid lines represent the median value for each one of the plotted quantities and the dashed lines the +/- 1 per cent scatter.

ρ_{gas} [$10^{15}h^{-1}$M$_{SUN}$Mpc^{-2}]
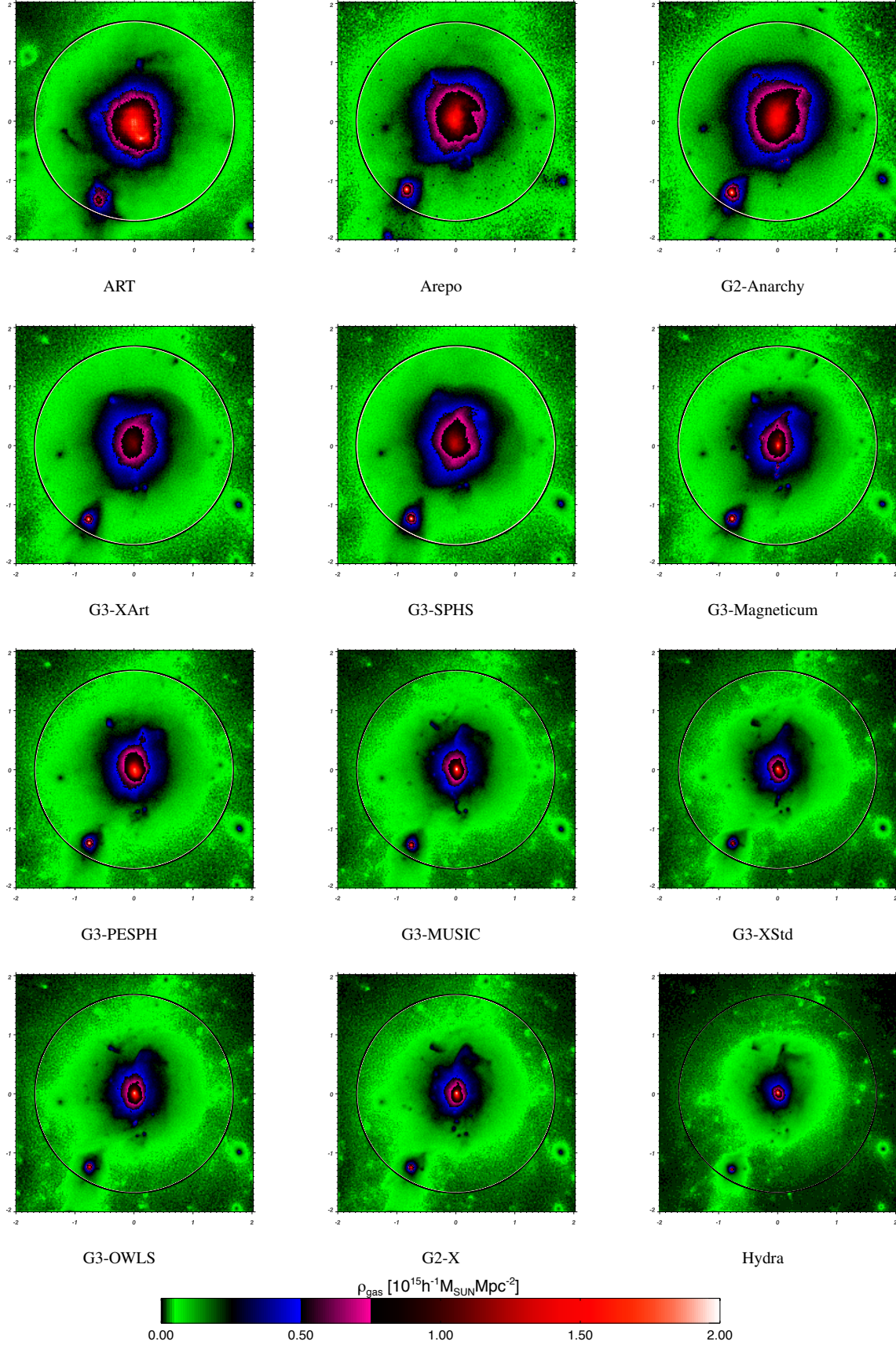
Figure 5. Projected density of the gas halo at $z = 0$ for each simulation as indicated. The box is $2h^{-1}$Mpc on a side. The white circle indicates M_{200}^{crit} for the halo, the black circle shows the same but for the G3-MUSIC simulation.
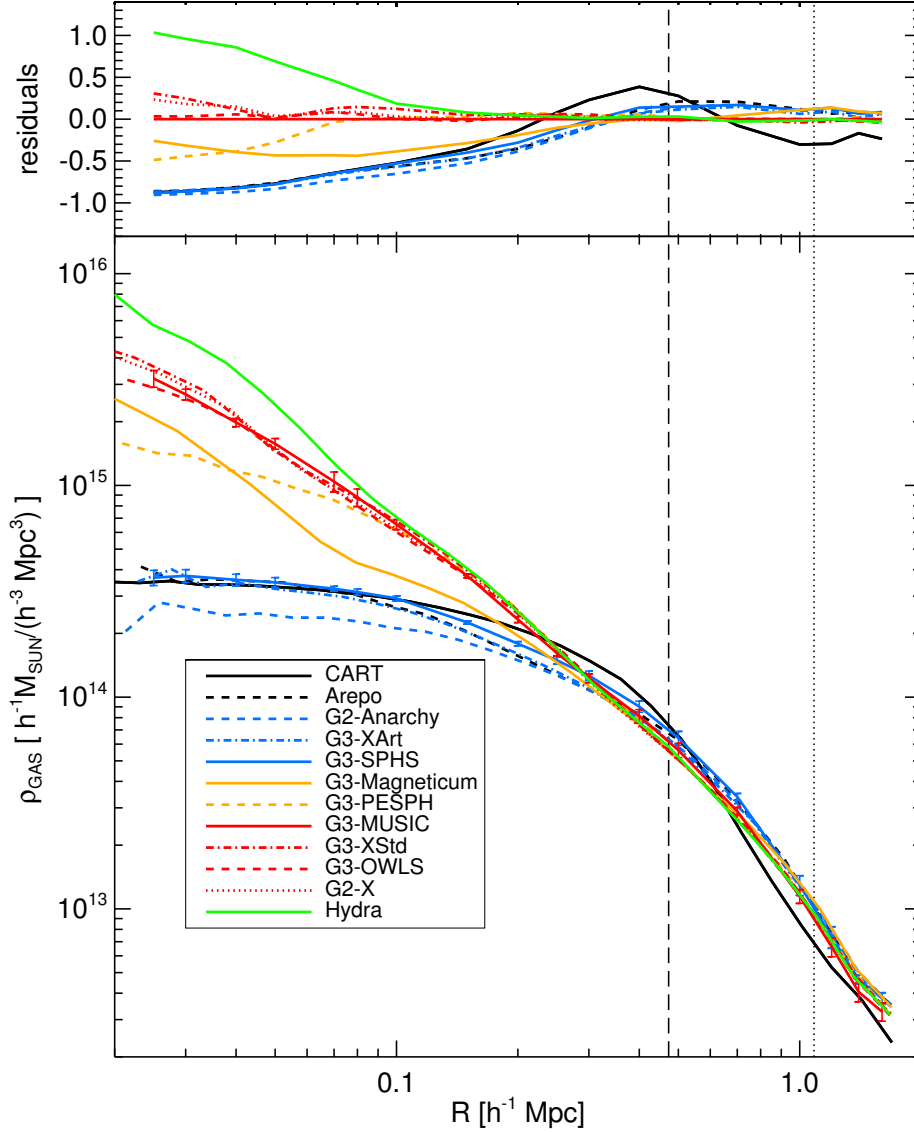
Figure 6. Radial gas density profiles at $z = 0$ for each simulation as indicated (bottom panel) and difference in radial gas density profiles at $z = 0$ between each simulation and the reference G3-MUSIC simulation . The vertical dashed line corresponds to R_{2500} and the dotted line to R_{500} of the reference G3-MUSIC values. The error bars on G3-SPHS (black) and G3-MUSIC (red) are calculated from the scatter between snapshots averaged over 0.27 Gyrs. The data are cut off when the radius goes below the softening scale of the code.

are matched (see Appendix). However, even the 'matched' simulations show important phase differences between simulations (Figure A1). The numerous implementations of GADGET agree remarkably well, but this is perhaps not surprising given that the gravity solver is in each case built on the same foundation. CART, however, shows a marked disagreement, as a large sub halo appears to be absent. Similar results were reported recently in Power, Read & Hobbs (2014) when comparing G3-SPHS with the RAMSES AMR code (see their Figure 7). It is not clear that this is either a problem or unexpected. We are, after all, modeling a chaotic system and while we can expect the *statistics* of the density field to agree between codes, it is likely unreasonable to expect the precise merger history and merger phase to agree between codes for a single object. Ideally, we would compare the halo statistics between codes for a large ensemble of cluster zoom simulations. Such a study is

beyond the scope of this present work and will treated in an future paper dedicated to the study of the subhalos.

6.2 Adding gas: AMR versus SPH

Issues such as the merger phase appear to affect the resulting dark matter properties at the ~ 10 per cent level (Figures 2-3). However, once adding gas, the merger phase produces a larger effect than this on the resulting gas distribution. This is because entropy in clusters is generated in shocks during collapse and mergers (Mitchell et al., 2009; Power, Read & Hobbs, 2014). The different codes explored here broadly fall into four categories. There are the 'classic' SPH methods (HYDRA; G3-MUSIC; G3-OWLS; G3-XStd; G2-X); the 'modern' SPH methods that attempt to correct for problems with mixing in classic SPH (G3-XArt; G3-SPHS; G2-Anarchy; G3-
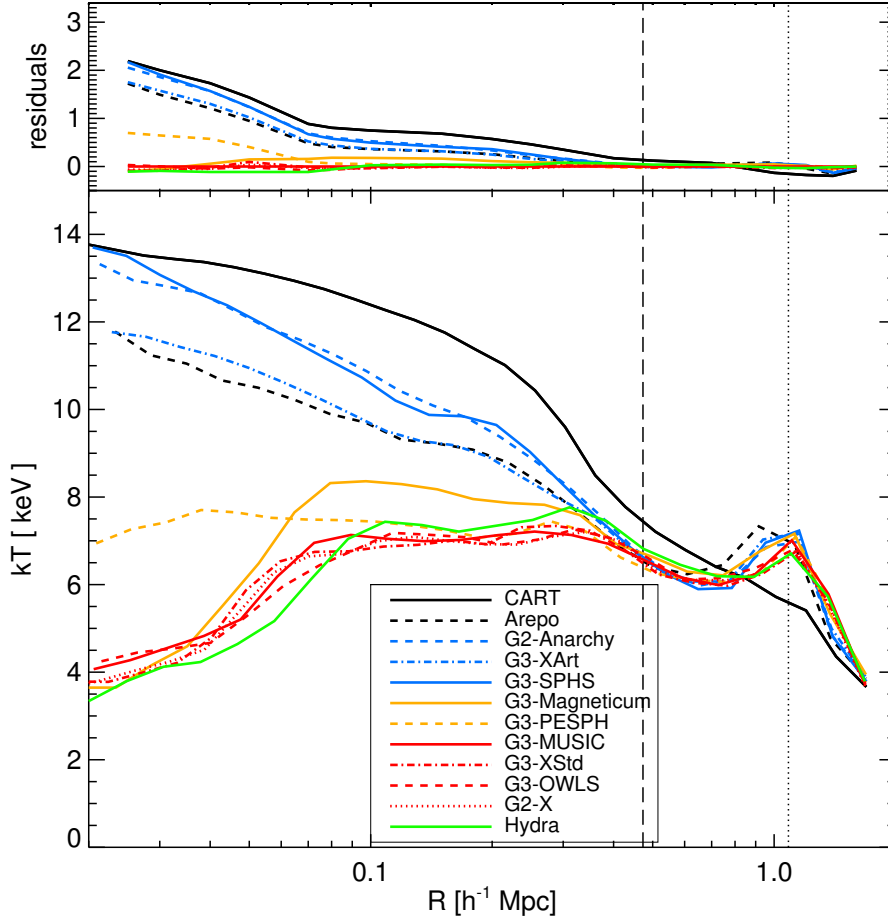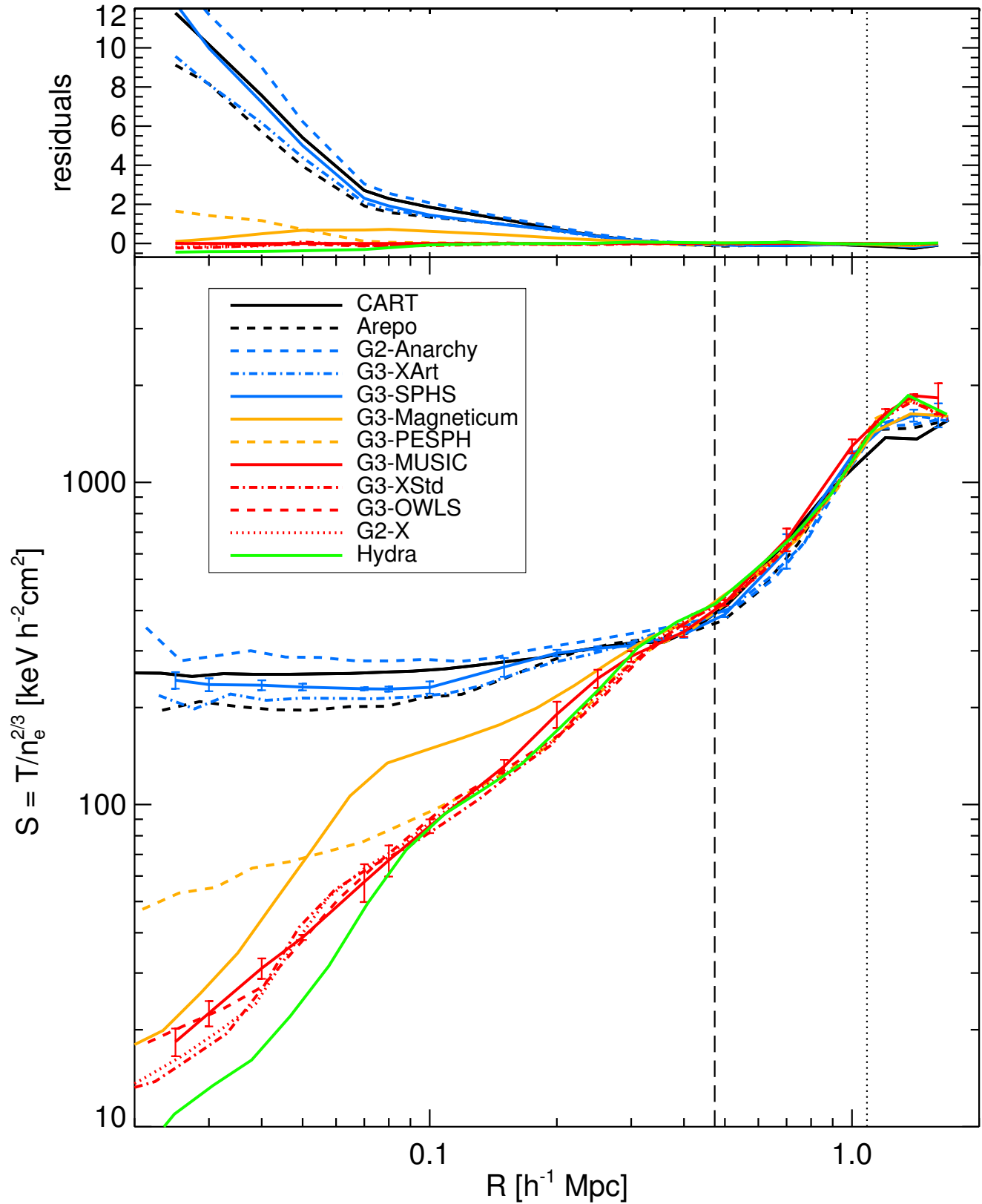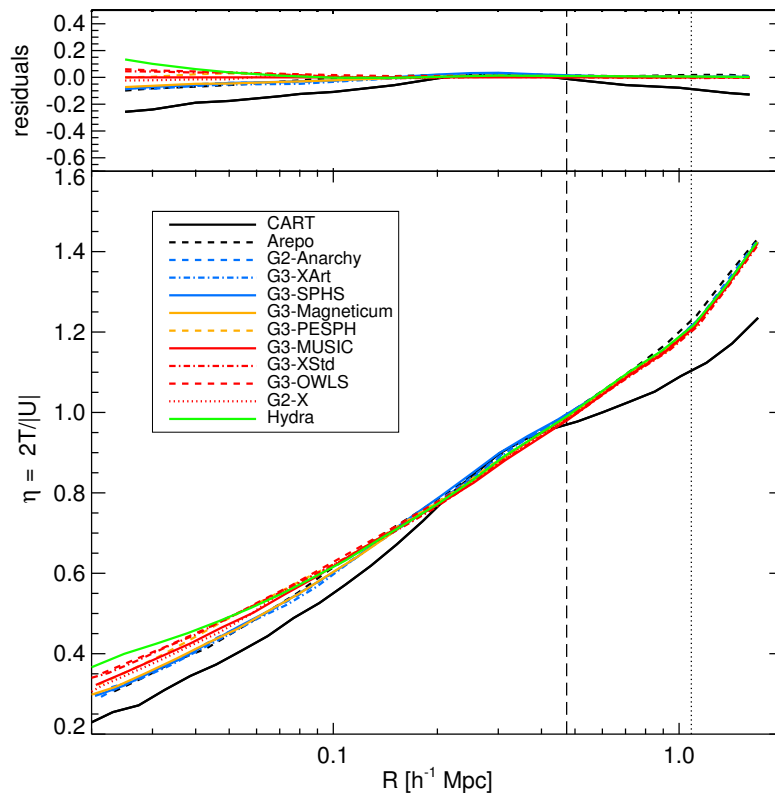
Figure 7. Radial temperature profile at $z = 0$ for each simulation as indicated and difference between each simulation and the reference G3-MUSIC simulation. The vertical dashed line corresponds to R_{2500} and the vertical dotted line to R_{500} of the reference G3-MUSIC values.

PESPH; G3-Magneticum); an Adaptive Mesh refinement method (CART) and a hybrid 'moving mesh' method (AREPO; see section 2 for further details of each method and the differences between them). The AMR code CART that is the most discrepant in its dark matter distribution is also the most discrepant in in its gas distribution, particularly at large radii. This is almost certainly attributable to the different merger phase, as can be seen from Figure A1.

6.3   The trouble with 'classic' SPH

Despite the excellent agreement between the 'dark matter only' runs, the classic SPH simulations also show scatter in their central gas density, temperature and entropy that is significantly larger than the theoretical error on each (as calculated from the scatter between snapshots averaged over 0.27 Gyrs; see the error bars marked on the plots shown in Figures 6 and 8). This is likely because in classic SPH, low entropy particles artificially sink to the cluster centre due to the lack of mixing (Power, Read & Hobbs, 2014), amplifying the effect of small changes in merger phase. We see this in Figure 5.

6.4   Modern SPH and AREPO

Of considerable interest are the differences between the modern SPH flavors (G3-XArt; G3-SPHS; G2-Anarchy; G3-PESPH; G3-Magneticum) and the moving mesh code AREPO. There is excel-

lent agreement between the dark matter distributions across the runs, which allows us to isolate the effect of the hydrodynamics solver (Figure A1). For the gas distributions shown in Figure 6, AREPO G3-XArt and G3-SPHS are in excellent agreement with one another, agreeing almost perfectly within our estimated theoretical error, while G2-Anarchy seems to be the outlier. In Figure 7 the temperature profiles for AREPO and G3-XArt are very closely matched but look to have an offset from G3-SPHS and G2-Anarchy, which are very close to one other. In Figure 8 the radial entropy profiles of G3-SPHS, G3-XArt and AREPO are again very close to one another while G2-Anarchy is more discrepant, though closer to CART. The origin of these differences is yet to be explained, although we note that it cannot be attributed to different merger phases and must result from the hydrodynamics solver. In the case of G2-Anarchy a possible cause of discrepancy may be the choice of the kernel (using a C4 kernel with 200 neighbors gives slightly different values for the central entropy). Power, Read & Hobbs (2014) showed that at the resolution of the simulations in this paper, G3-SPHS is numerically converged. It would be interesting to see if the differences between G3-SPHS/G3-XArt/Arepo and G2-Anarchy remain with increasing resolution. We defer such a resolution study to future work, whose intent will be to narrow down these numerical uncertainties.

In the Arepo simulations we have used the total energy as a conserved quantity in the Godunov scheme, which is the usual

Figure 8. Radial entropy at $z = 0$ (bottom panel) for each simulation as indicated and difference between each simulation and the reference G3-MUSIC simulation (top panel). The dashed line corresponds to R_{2500} and the dotted line to R_{500} of the reference G3-MUSIC values. The error bars on G3-SPHS (black) and G3-MUSIC (red) are calculated from the scatter between snapshots averaged over 0.27 Gyrs.

Figure 9. The ratio of kinetic to thermal energy in the gas, η, measured radially at $z = 0$ for each simulation as indicated (top) and difference between each simulation and the reference G3-MUSIC simulation (bottom). Dashed line corresponds to R_{2500} and dotted line to R_{500} of the reference G3-MUSIC values.

choice in finite volume codes and has been used in most recent Arepo studies (as, e.g., in Vogelsberger et al. 2014). As discussed in Springel (2010), using an entropy-energy formalism results in smaller entropy cores and higher central gas densities somewhat closer to classic SPH results (similar results are also shown by GIZMO, Hopkins 2014). Following most recent Arepo studies, we have not employed the later method here due to concerns regarding the artificial suppression of weak shocks and the potentially less accurate energy conservation.

Finally, we note that the results of G3-PESPH are very different from those of the other modern SPH flavours (with the exception of G3-Magneticum), and are more similar to those of classic SPH simulations. A key difference is that this version of G3-PESPH does not include any explicit conductivity or mixing, while all the other modern variants do. Hu et al. (2014) showed that PESPH performs much better than previous versions of SPH for surface instabilities by greatly mitigating surface tension problems, but in areas of very strong shocks (M~1000) adding artificial conduction provides a better match to analytic solutions. Insights into the behavior of G3-PESPH may be gained by considering the OSPH method presented in Read, Hayfield & Agertz (2010), and the earlier multiphase RT method by Ritchie & Thomas (2001). As pointed out by Read & Hayfield (2012a), the RT method only works well for relatively small entropy contrasts between different fluid phases. As the entropy contrast becomes very large, the admixture of low and high entropy particles within the smoothing kernel creates large pressure fluctuations that prevent mixing, as in classic SPH. This was recognized also by Ritchie & Thomas (2001) who proposed scaling the neighbor number with the entropy contrast to combat this. However, this rapidly becomes prohibitively expen-

sive in realworld applications, which led Read & Hayfield (2012a) to abandon such RT methods in favor of dissipation switching, as proposed by Price (2008); such switching is common to G3-XArt, G3-SPHS and G2-Anarchy and helps to explain their similarity. The discrepancy between G3-PESPH and the other modern SPH flavours may also reflect the treatment of artificial viscosity adopting the artificial viscosity model suggested by Cullen & Dehnen (2010) can produce larger entropy gains in shocks, but the authors of G3-PESPH do not use this because it also seems to add substantial entropy into very diffuse intergalactic gas that may be spurious (N. Katz, priv. comm.). In short, it is unclear how much artificial conductivity and/or mixing is appropriate in SPH, or even whether the mesh codes are providing the correct solution that all SPH codes should be trying to emulate. Nonetheless, consistency with mesh codes appears to require modern SPH using conduction, mixing, and/or a higher-order dissipation switch.

The discrepancy between G3-PESPH and the other modern SPH flavours may also reflect the treatment of artificial viscosity – adopting the artificial viscosity model suggested by Cullen & Dehnen (2010) should lead to a better agreement with mesh-based codes.

7 SUMMARY & CONCLUSIONS

We have investigated the performance of 12 modern astrophysical simulation codes – CART, HYDRA, AREPO and 9 versions of GADGET with different SPH implementations – by carrying out cosmological zoom simulations of a single massive galaxy cluster. Our goal was to assess the consistency of the different codes in re-
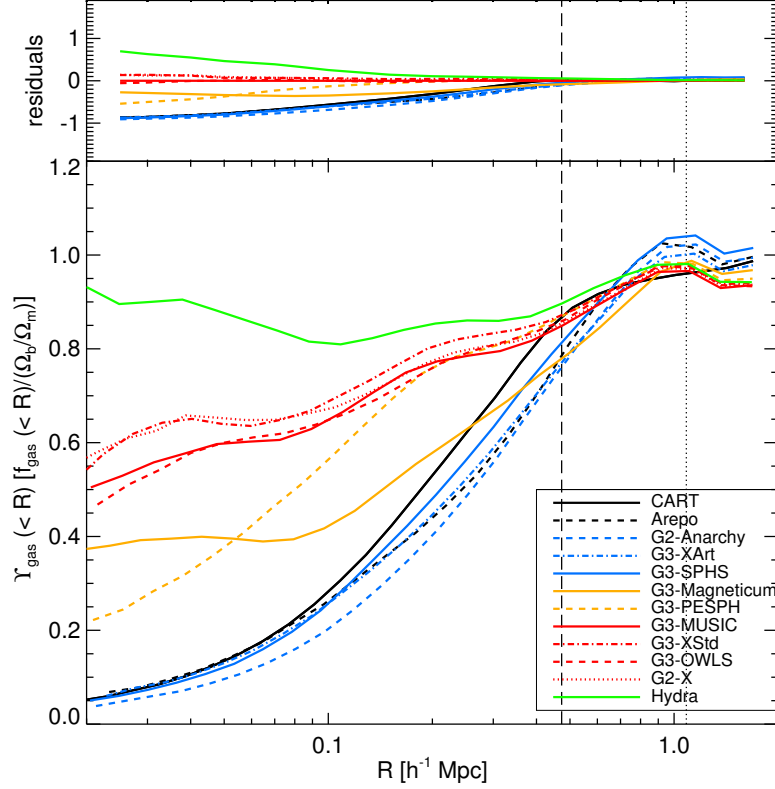
Figure 10. Radial gas fraction at $z = 0$ relative to the cosmic value for each simulation as indicated (top) and difference between each simulation and the reference G3-MUSIC simulation (bottom). The dashed vertical line corresponds to R_{2500} and dotted vertical line to R_{500} of the reference G3-MUSIC values.

producing the spatial and thermodynamical structure of dark matter and non-radiative gas in the cluster.

As our initial step, we ran dark matter only versions of the simulations with each code using its preferred set of numerical parameters (e.g. time step accuracy, gravitational softening, dimension of the particle mesh), and examined the spherically averaged mass density profile and the spatial distribution of substructures. We found good consistency between the density profiles recovered by the codes at approximately the 10 per cent level, while there were small variations in the positions of substructures. When these simulations were re-run with a common set of numerical parameters, we found that these small variations could be suppressed (essentially entirely, in the case of the GADGET codes).

By adopting this common parameter set, we were able to isolate those differences between the results of the hydrodynamical simulations that arise only from the choice of hydrodynamical solver, rather than from the complex interplay of the hydrodynamical and gravity solvers. Interestingly, we found that the resulting gas density profiles varied substantially amongst the codes. Our key findings can be summarized as follows:

- Some codes, essentially the oldest, with classic SPH implementations, exhibit continually falling inner entropy profiles, without any evidence of an entropy core. This is because these codes, particularly HYDRA ,were carefully designed to be entropy conserving with very low levels of mixing. This lack of mixing preserves low-entropy gas particles at the centers of all objects, including subhalos, which survive until late times. As the cluster relaxes, these particles sink to the centre of the radial density profile, decreasing the central entropy.

- In contrast, the grid-based codes CART and AREPO produce extended cores with a large constant entropy core. In these mesh based codes mixing of entropy arises as a consequence of the numerical diffusion associated with the Riemann solver: they naturally mix entropy between gas elements, essentially eliminating the very low entropy material.

- Modern SPH codes such as G3-ANARCHY, G3-SPHS and G3-XART, which have dissipative switches and new kernels, can bridge the gap between the classic SPH codes and grid based codes, and produce entropy cores that are indistinguishable from those of the grid-based codes.

Our results confirm that the discrepancies between grid-based codes and SPH codes in describing the radial entropy profile of simulated clusters, identified by the Santa Barbara comparison project presented in Frenk et al. (1999), can be overcome by modern SPH codes. Importantly, all the codes employed in this work succeed in recovering the global properties and most of the radial profiles of a simulated large galaxy cluster with much greater accuracy and significantly smaller scatter than those presented in Frenk et al. (1999); this highlights the enormous strides in the development of astrophysical hydrodynamical simulation codes over the last decade.

This work constitutes the first in a series of papers in which we examine in detail the predictions of modern astrophysical hydrodynamical simulation codes. The next paper in this series will focus on simulations of the same galaxy cluster, now modeled with a variety of galaxy formation processes including cooling, star formation, supernovae, and feedback from active galactic nuclei (AGN). This will allow us to establish how radiative processes affect the entropy cores of simulated clusters. Subsequent papers will look at
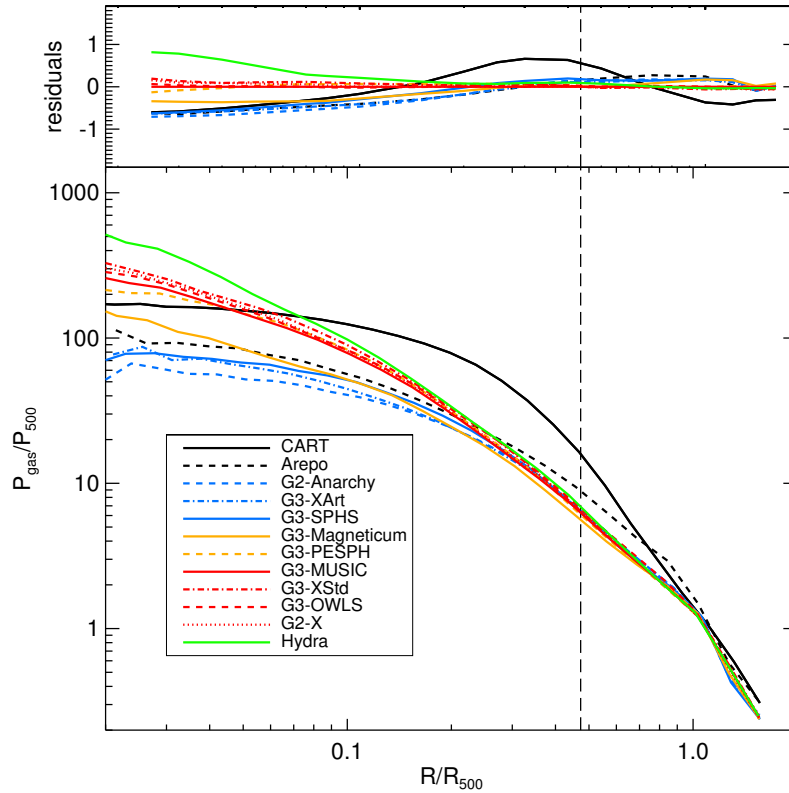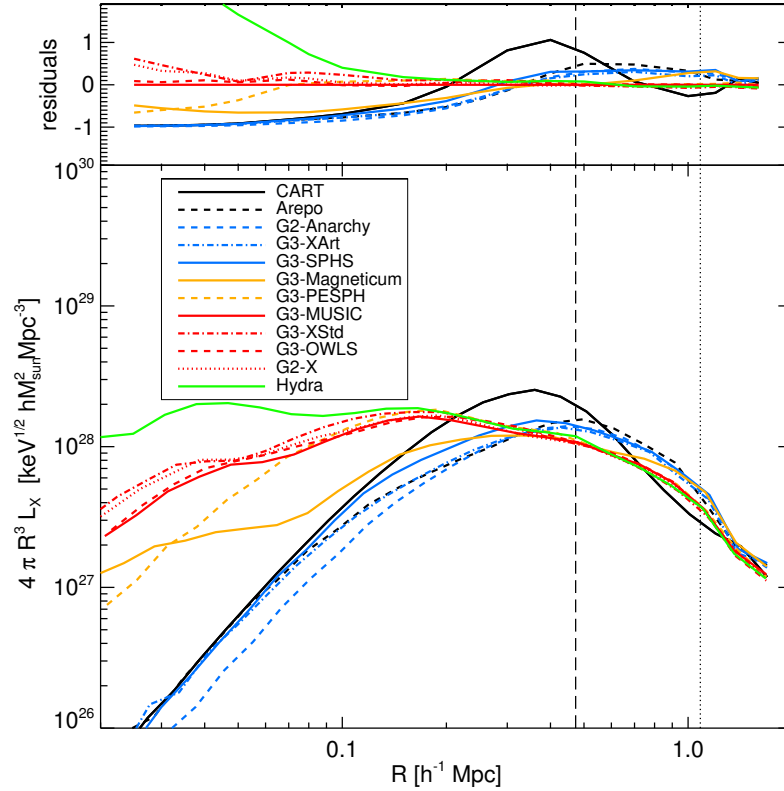
Figure 11. Radial gas pressure at $z = 0$ measured in each simulation as indicated (bottom panel) and difference between each simulation and the reference G3-MUSIC simulation (top panel). The pressure, as well as the radius, has been normalized to the corresponding value at R_{500} for each code. The dashed vertical line corresponds to R_{2500} of the reference G3-MUSIC value.

the recovery of cluster properties such as X-ray temperature and Sunyaev-Zel'dovich profiles; gravitational lensing; and cluster outskirts and hydrostatic mass bias; all of which will add to our understanding of how consistently the results of different codes can inform our understanding of galaxy cluster properties.

Figure 12. Radial X-ray luminosity profiles at $z = 0$ for each simulation as indicated (bottom panel) and difference between each simulation and the reference G3-MUSIC simulation (top panel)..The dashed vertical line corresponds to R_{2500} of the reference G3-MUSIC value.

with resources awarded through STFCs DiRAC initiative. The authors thank Volger Springel for helpful discussions and for making AREPO and the original GADGET version available for this project.

The authors contributed to this paper in the following ways: FS, GY, FRP, AK, CP, STK & WC formed the core team that organized and analyzed the data, made the plots and wrote the paper. AK, GY & FRP organized the nIFTy workshop at which this program was completed. GY supplied the initial conditions. PJE assisted with the analysis. All the other authors, as listed in Section 2 performed the simulations using their codes. All authors had the opportunity to proof read and comment on the paper.

The simulation used for this paper has been run on Marenostrum supercomputer and is publicly available at the MUSIC website[4].

This research has made use of NASA's Astrophysics Data System (ADS) and the arXiv preprint server.

References

Aarseth S. J., Turner E. L., Gott, III J. R., 1979, ApJ, 228, 664
Agertz O. et al., 2007, MNRAS, 380, 963
Allen S. W., Evrard A. E., Mantz A. B., 2011, ARA&A, 49, 409
Arnaud M., Pratt G. W., Piffaretti R., Böhringer H., Croston J. H., Pointecouteau E., 2010, A&A, 517, A92
Balsara D. S., 1995, Journal of Computational Physics, 121, 357

Beck A. M. et al., 2015, ArXiv e-prints
Biffi V., Sembolini F., De Petris M., Valdarnini R., Yepes G., Gottlöber S., 2014, MNRAS, 439, 588
Booth C. M., Schaye J., 2009, MNRAS, 398, 53
Borgani S., Kravtsov A., 2011, Advanced Science Letters, 4, 204
Borgani S. et al., 2004, MNRAS, 348, 1078
Colella P., Glaz H. M., 1985, Journal of Computational Physics, 59, 264
Couchman H. M. P., Thomas P. A., Pearce F. R., 1995, ApJ, 452, 797
Cullen L., Dehnen W., 2010, MNRAS, 408, 669
Dalla Vecchia C., Schaye J., 2012, MNRAS, 426, 140
Davé R., Katz N., Weinberg D. H., 2002, ApJ, 579, 23
Davé R., Oppenheimer B. D., Sivanandam S., 2008, MNRAS, 391, 110
Dehnen W., Aly H., 2012, MNRAS, 425, 1068
Di Matteo T., Springel V., Hernquist L., 2005, Nature, 433, 604
Dolag K., Jubelgas M., Springel V., Borgani S., Rasia E., 2004, ApJ, 606, L97
Dolag K., Vazza F., Brunetti G., Tormen G., 2005, MNRAS, 364, 753
Durier F., Dalla Vecchia C., 2012, MNRAS, 419, 465
Fall S. M., 1978, MNRAS, 185, 165
Frenk et al. C. S., 1999, ApJ, 525, 554
Gill S. P. D., Knebe A., Gibson B. K., 2004, MNRAS, 351, 399
Gingold R. A., Monaghan J. J., 1977, MNRAS, 181, 375
Hirschmann M., Dolag K., Saro A., Bachmann L., Borgani S., Burkert A., 2014, MNRAS, 442, 2304
Hopkins P. F., 2013, MNRAS, 428, 2840
Hopkins P. F., 2014, ArXiv e-prints

---

[4] http://music.ft.uam.es

Hu C.-Y., Naab T., Walch S., Moster B. P., Oser L., 2014, MN-RAS, 443, 1173

Kay S. T., Thomas P. A., Jenkins A., Pearce F. R., 2004, MNRAS, 355, 1091

Klypin A., Kravtsov A. V., Bullock J. S., Primack J. R., 2001, ApJ, 554, 903

Knollmann S. R., Knebe A., 2009, ApJS, 182, 608

Komatsu E. et al., 2011, ApJS, 192, 18

Kravtsov A. V., Borgani S., 2012, ARA&A, 50, 353

Kravtsov A. V., Klypin A. A., Khokhlov A. M., 1997, ApJS, 111, 73

Le Brun A. M. C., McCarthy I. G., Schaye J., Ponman T. J., 2014, MNRAS, 441, 1270

Lucy L. B., 1977, AJ, 82, 1013

Maier A., Iapichino L., Schmidt W., Niemeyer J. C., 2009, ApJ, 707, 40

Metzler C. A., Evrard A. E., 1994, ApJ, 437, 564

Mitchell N. L., McCarthy I. G., Bower R. G., Theuns T., Crain R. A., 2009, MNRAS, 395, 180

Monaghan J. J., 1997, Journal of Computational Physics, 136, 298

Monaghan J. J., Lattanzio J. C., 1985, A&A, 149, 135

Morris J. P., Monaghan J. J., 1997, Journal of Computational Physics, 136, 41

Muanwong O., Thomas P. A., Kay S. T., Pearce F. R., Couchman H. M. P., 2001, ApJ, 552, L27

Nagai D., Vikhlinin A., Kravtsov A. V., 2007, ApJ, 655, 98

O'Shea B. W., Nagamine K., Springel V., Hernquist L., Norman M. L., 2005, ApJS, 160, 1

Pakmor R., Edelmann P., Röpke F. K., Hillebrandt W., 2012, MN-RAS, 424, 2222

Pearce F. R., Thomas P. A., Couchman H. M. P., Edge A. C., 2000, MNRAS, 317, 1029

Pike S. R., Kay S. T., Newton R. D. A., Thomas P. A., Jenkins A., 2014, MNRAS, 1, 1

Power C., Read J. I., Hobbs A., 2014, MNRAS, 440, 3243

Prada F., Klypin A. A., Cuesta A. J., Betancort-Rijo J. E., Primack J., 2012, MNRAS, 423, 3018

Price D. J., 2008, J. Comp. Phys., 227, 10040

Price D. J., 2012, Journal of Computational Physics, 231, 759

Puchwein E., Sijacki D., Springel V., 2008, ApJ, 687, L53

Read J. I., Hayfield T., 2012a, MNRAS, 422, 3037

Read J. I., Hayfield T., 2012b, MNRAS, 2941

Read J. I., Hayfield T., Agertz O., 2010, MNRAS, 405, 1513

Ritchie B. W., Thomas P. A., 2001, MNRAS, 323, 743

Rudd D. H., Zentner A. R., Kravtsov A. V., 2008, ApJ, 672, 19

Saitoh T. R., Makino J., 2013, ApJ, 768, 44

Schaye J., Dalla Vecchia C., 2008, MNRAS, 383, 1210

Schaye J. et al., 2010, MNRAS, 402, 1536

Sembolini F., De Petris M., Yepes G., Foschi E., Lamagna L., Gottlöber S., 2014, MNRAS, 440, 3520

Sembolini F., Yepes G., De Petris M., Gottlöber S., Lamagna L., Comis B., 2013, MNRAS, 429, 323

Sijacki D., Pfrommer C., Springel V., Enßlin T. A., 2008, MN-RAS, 387, 1403

Sijacki D., Springel V., Di Matteo T., Hernquist L., 2007, MN-RAS, 380, 877

Sijacki D., Vogelsberger M., Kereš D., Springel V., Hernquist L., 2012, MNRAS, 424, 2999

Springel V., 2005, MNRAS, 364, 1105

Springel V., 2010, MNRAS, 401, 791

Springel V., Hernquist L., 2002, MNRAS, 333, 649

Springel V., Hernquist L., 2003, MNRAS, 339, 289

Teyssier R., 2002, A&A, 385, 337

Thacker R. J., Couchman H. M. P., 2006, Computer Physics Communications, 174, 540

Thacker R. J., Scannapieco E., Couchman H. M. P., 2006, ApJ, 653, 86

Tricco T. S., Price D. J., 2013, MNRAS, 436, 2810

Vogelsberger M. et al., 2014, Nature, 509, 177

Voit G. M., Kay S. T., Bryan G. L., 2005, MNRAS, 364, 909

Wadsley J. W., Veeravalli G., Couchman H. M. P., 2008, MNRAS, 387, 427

Wendland H., 1995, Advances in Computational Mathematics, 4, 389

White S. D. M., 1976, MNRAS, 177, 717

Wiersma R. P. C., Schaye J., Smith B. D., 2009, MNRAS, 393, 99

8   DARK MATTER ALIGNMENT

In order to perform a clean comparison of the various gas physics implementations we carefully aligned the underlying gravitational framework for each model. While Figure 1 illustrates the range of outcomes that result from a blind comparison using individual parameter choices, we can choose a common parameter set for those quantities that control the accuracy of the gravitational forces. For instance, for GADGET, Table 4 gives the parameter choices made independently by each group. The final row lists the common parameter set adopted for the non-radiative comparison. For this common choice the gravitational evolution of the nine GADGET simulations and AREPO is, as expected, essentially indistinguishable, as illustrated by Figure 13. Figure 14 shows the radial density distribution and the difference relative to the G3-MUSIC simulation. For HYDRA, the central gas density is so high that it steepens the central dark matter distribution relative to the other codes.
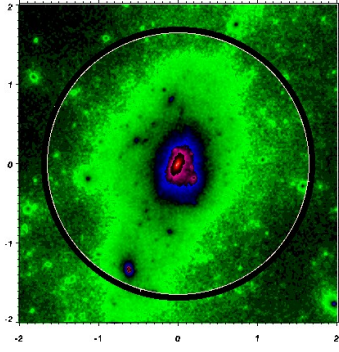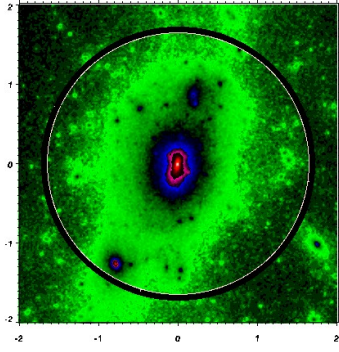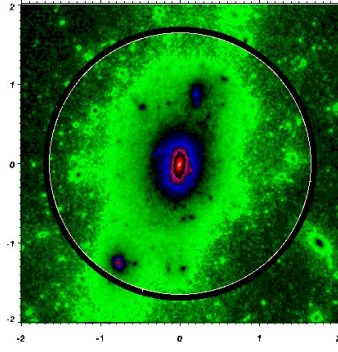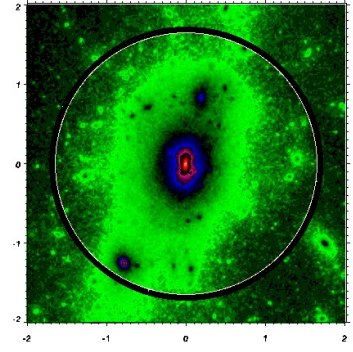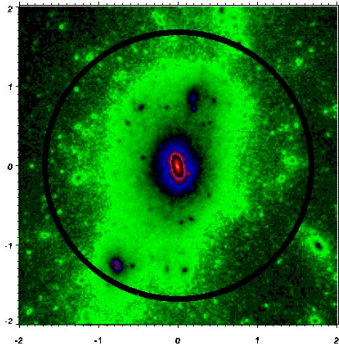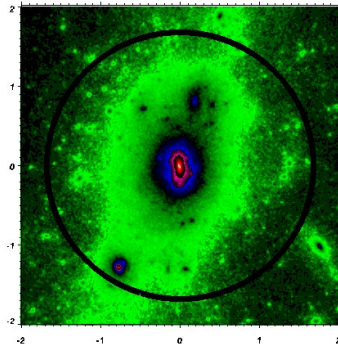
CART
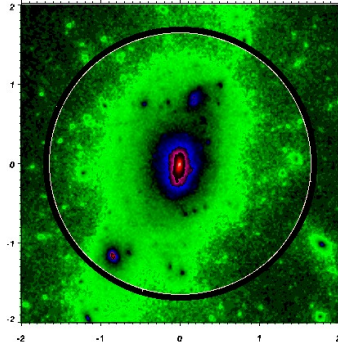
Arepo
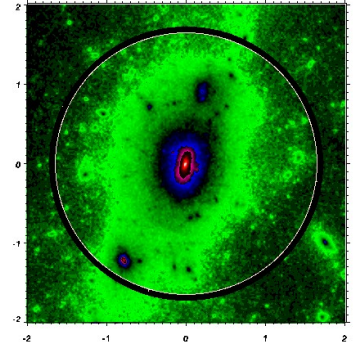
G2-Anarchy

G3-XArt

G3-SPHS

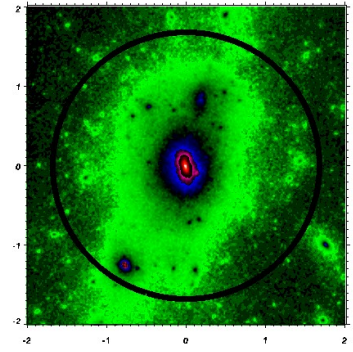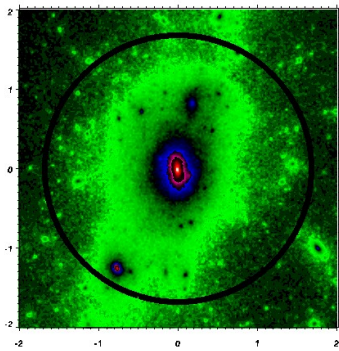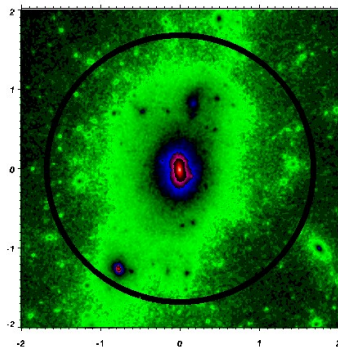G3-Magneticum

G3-PESPH

G3-MUSIC
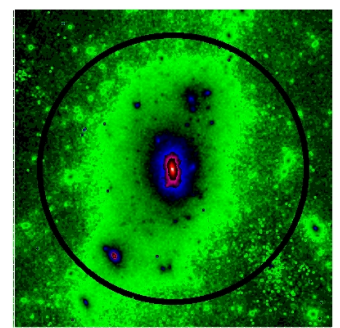
G3-XStd

G3-OWLS

G2-X

Hydra

ρ_{DM} [$10^{15}h^{-1}M_{SUN}Mpc^{-2}$]

Table 4. Numerical parameters used for the AREPO and GADGET runs: accuracy of the time step (ETIA), time step displacement factor (MRDF), minimum (MINT) and maximum (MAXT) time step, tolerance on the force accuracy (ETFA), accuracy of the tree algorithm (ETT), Courant factor (CFAC) and double precision (DP, DF).

| Code name	ETIA	MRDF	MINT	MAXT	ETFA	ETT	CFAC	DP	DF
AREPO	0.025	0.125	0	0.01	0.0025	0.6	0.3	Y	Y
GADGET2-X	0.02	0.25	10^{-7}	0.025	0.0025	0.3	0.15	Y	Y
GADGET3-MAGNETICUM	0.05	0.25	0	0.05	0.005	0.45	0.15	Y	Y
GADGET3-MUSIC	0.01	0.5	0	0.01	0.01	0.4	0.15	Y	Y
GADGET3-OWLS	0.025	0.25	10^{-10}	0.025	0.005	0.6	0.15	Y	N
GADGET3-SPHS	0.03	0.5	0	0.02	0.005	0.5	0.4	N	N
GADGET3-X	0.01	0.5	0	0.01	0.01	0.45	0.15	N	N
GADGET3-PESPH	0.05	0.25	10^{-7}	0.05	0.005	0.4	0.15	Y	Y
GADGET2-ANARCHY	0.01	0.125	0.0	0.01	0.025	0.3	0.3	Y	Y
Common parameter set	0.01	0.125	0.0	0.01	0.025	0.3	0.15	Y	Y
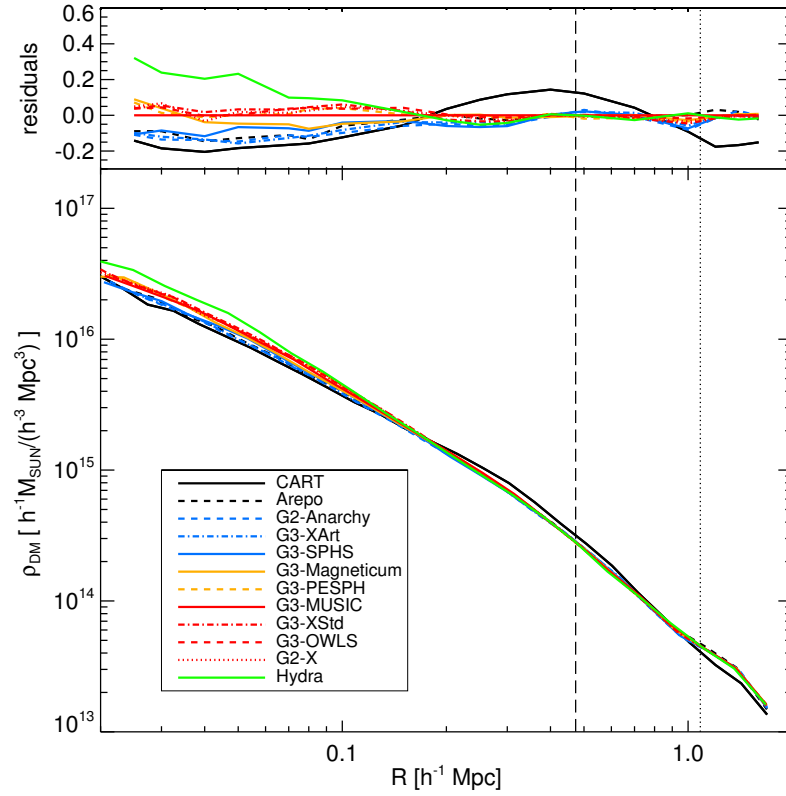
Figure 14. Radial density profiles for the non radiative simulations at $z = 0$ (bottom panel) and difference between the radial density profiles of each non radiative simulations at $z = 0$ and the reference G3-MUSIC density profile (top panel). The vertical dashed line corresponds to R_{2500} and the vertical dotted line to R_{500} of the reference G3-MUSIC values.